Structural evolution of α-Fe$_2$O$_3$ nanowires during lithiation and delithiation

Bo Huang, Kaiping Tai, Shen J. Dillon*

Department of Materials Science and Engineering, University of Illinois Urbana-Champaign, Urbana, IL, USA

HIGHLIGHTS

- Fe$_3$O$_4$ nanocrystals form as intermediate products during lithiation.
- Size of nanocrystals evolve at various lithiation and delithiation stages.
- Fe$_2$O$_3$ is regained in the form of nanocrystals after delithiation.
- Li diffuses into the nanowire with Fe and O remain within the nanowire boundary.
- Nanowires geometrically persistent over multiple cycles.

ARTICLE INFO

ABSTRACT

This work describes the evolution of α-Fe$_2$O$_3$ nanowires during the conversion reaction associated with lithium intercalation. An electrical resistive heating method synthesizes single crystal hematite (α-Fe$_2$O$_3$) nanowires. Transmission electron microscopy characterizes this anode material at various stages of lithiation and delithiation. The process initiates through the reduction of α-Fe$_2$O$_3$ to nanocrystalline Fe$_3$O$_4$. Further lithiation converts all of the iron oxide to nanocrystalline BCC Fe. During delithiation, the reactions proceed via conversion of Fe^0 to Fe$_2$O$_3$. However, a nanocrystalline structure replaces the initial single crystalline α-Fe$_2$O$_3$ after the first circle. This polycrystalline nanowire structure persists for over 30 cycles.

1. Introduction

Various schemes for realizing high capacity electrode materials for lithium ion batteries have been proposed and investigated in the past two decades to meet growing demand for portable and mobile energy storage [1–5]. Electrodes may accommodate lithium through intercalation, alloying, or conversion reactions. Intercalation electrodes typically exhibit relatively low capacities, due to constraints imposed by crystal structure and valence changes. Alloying electrodes possess large capacities, but typically exhibit large strains and associated degradation processes that limit their cycle life [6–10]. The voltage window of alloying electrodes prohibit their use as practical cathodes and therefore only provide limited improvement to overall energy density of cells containing low capacity cathodes. Conversion reaction electrodes have large capacities and could function as either anodes or cathodes, depending on their chemistry. However, they exhibit significant hysteresis that limits their efficiency and may be reasonably susceptible to capacity fade. If novel nanostructuring approaches could be realized to improve the reversibility and reduce the hysteresis associated with conversion reactions, significant improvements in the energy density of lithium ion batteries might be realized. Here we seek to characterize the nanostructural evolution of a model conversion reaction electrode, α-Fe$_2$O$_3$, in order to gain improved insights into the mechanisms associated with the process.

The chemical reaction associated with lithiation and delithiation of conversion electrodes may be expressed generally as [11]:
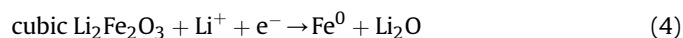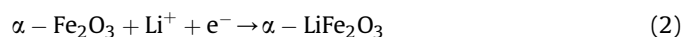
* Corresponding author.
   E-mail addresses: bohuang2@illinois.edu, huangboscu@163.com (B. Huang), kptai@illinois.edu (K. Tai), sdillon@illinois.edu (S.J. Dillon).

$$M_xO + 2Li^+ + 2e^- \leftrightarrow Li_2O + xM(M = Fe, Ni, Cu, Co, etc.) \quad (1)$$
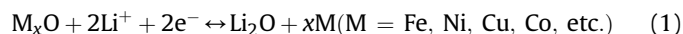
Similar reactions may also be realized through the use of alternative anions. Li_2O forms and decomposes during each cycle accompanied by the reduction and oxidation of metallic nanoparticles [11]. Large hysteresis likely results from the poor electronic conductivity of Li_2O, the necessity for low temperature cation diffusion in oxide phases, and the activation barrier associated with nucleating a new phase. All three processes benefit from the use nanostructured phases with limited transport length scales and high surface area.

Fe_2O_3 has been widely studied due to its abundance, low cost, and interesting magnetic, semiconducting, and electrochemical properties [12–21]. According to in-situ X-ray diffraction studies performed by Larcher et al. [18,20], 20 nm Fe_2O_3 particles first accommodate lithium ions by forming a hexagonal $LiFe_2O_3$ phase. A phase transformation from a phase with a close-packed hexagonal anion lattice (α-$LiFe_2O_3$) to a disordered cubic structure ($Li_2Fe_2O_3$) occurs upon further lithiation. Iron nanoparticles (<2 nm determined from X-ray peak broadening) precipitate in an amorphous Li_2O matrix, which forms simultaneously during deep discharging. Equations (2)–(4) described the process proposed based on X-ray analysis [20]:

$$\alpha - Fe_2O_3 + Li^+ + e^- \rightarrow \alpha - LiFe_2O_3 \quad (2)$$

$$\alpha - LiFe_2O_3 + Li^+ + e^- \rightarrow cubic\ Li_2Fe_2O_3 \quad (3)$$

$$cubic\ Li_2Fe_2O_3 + Li^+ + e^- \rightarrow Fe^0 + Li_2O \quad (4)$$

The characteristic microstructural length scales associated with the process are deemed critical to the function of these electrodes. Particle size measurements based on X-ray diffraction may be strongly affected by others factors (e.g. strain, defects, or contamination), which motivate the need for a direct measurement. In this paper, we report a simple approach to growing α-Fe_2O_3 single crystal nanowires and characterization of the lithiation and delithiation process, sampled at different states of charge, in a binder and carbon free system, by transmission electron microscopy (TEM).

2. Experimental procedure

Single crystal α-Fe_2O_3 nanowires were synthesized by Joule heating of ~220 μm diameter iron wire (99.99%, Goodfellow) under ambient conditions [22]. The iron wire was cut to ~10 cm long pieces, cleaned in dilute hydrochloric acid (2% in volume) for several minutes, and rinsed by acetone, alcohol, and deionized water. AC power (~4 W at 60 Hz) was applied to the ends of the wire to induce oxidation for ~10 min. This produces a high density of high aspect ratio α-Fe_2O_3 nanowires.

Traditional electrodes were fabricated from commercial α-Fe_2O_3 nanopowder (Sigma–Aldrich, 30 nm). The powder was mixed with polyvinylidene fluoride (PVDF) and Super P carbon in a ratio of 7:2:1. The powders were dispersed in 1-methyl-2-pyrrolidinone in order to form slurry that was cast on a Cu current collector. These more traditional composite electrodes were fabricated to facilitate characterization of phase evolution by X-ray diffraction (XRD), since the substrate supported nanowires are difficult to characterize in this manner.

The electrochemical properties of the α-Fe_2O_3 samples were characterized in a glass vial cell within a dry Ar-filled glove box (Mbraun Labstar). The iron wire served as the current collector for the α-Fe_2O_3 nanowires on the surface. This was cycled against a metallic lithium counter electrode in ethylene carbonate (EC) dimethyl carbonate (DMC) (1:1 by volume) 1 M $LiPF_6$ electrolyte. The electrochemical tests were carried out using a computer-controlled potentiostat/galvanostat (SP200, Biologic Co.). Samples were cycled to different states of charge (0.9 V, 0.8 V, 0.7 V, 0.6 V and 0.5 V) by slow scan cyclic voltammetry (CV) performed at 50 μV s^{-1}. The slow scan rate was selected to allow the nanowires to approach equilibrium during cycling, without having to fully lithiate the dense underlying oxide. To investigate the fully lithiated and delithiated states, the samples were also maintained at a constant potential of 0.1 V and 2.0 V for 3 h, respectively, after the potential sweeps. All of the tested samples were washed by propylene carbonate (PC) and acetone, and then dried in the glove box.

The microstructures of the α-Fe_2O_3 nanowires were characterized by scanning electron microscopy (JEOL-6060LV), transmission electron microscopy (JEOL-2010Lab$_6$ and JEOL-2010Cryo), and electron energy loss spectroscopy (EELS) in the scanning transmission electron microscopy (JEOL-2010F EF-FEG). XRD (Philips Xpert 2) was performed on the composite electrodes.

The mean diameter of α-Fe_2O_3 nanowires were averaged based on measurements taken at the middle of each nanowire. All the nanocrystals in dark-field (DF) images were assumed to be approximately spherical and their diameters were calculated in terms of areas (S) measured from each particle ($D = 2^*\sqrt{S/\pi}$).

3. Results and discussion

Nanowires, several microns in length (Fig. 1a and b) with an average diameter of ~105 nm, emerge from an underlying dense oxide shell. The corresponding selected area electron diffraction (SAED) pattern (Fig. 1c) indicates that the Fe_2O_3 nanowire growth occurs along [110] axis [22], which is also confirmed by the d-spacing imaged by high-resolution TEM (Fig. 1d).

Fig. 2a depicts a cyclic voltammogram acquired at a sweep rate of 500 μV s^{-1} in the range of 0.25–2.5 V. A small pre-peak and shoulder peak emerge near 0.9 V and a primary lithiation peak occurs near 0.7 V. A single delithiation peak appears near 1.7 V. The delithiation peaks are relatively broad, which likely results from the sluggish oxidation kinetics.

Reddy et al. [21] have reported CV results for α-Fe_2O_3 nanoflakes up to 15 cycles at a sweep rate of 58 μV s^{-1}, in which the reduction and oxidation peak appear at 1.0 and 2.0 V, respectively. Chen et al. [16] published the results of 20 CV cycles performed at 500 μV s^{-1} where the reduction and oxidation peaks occur at 0.5 and 2.1 V, respectively. Our current results fall within a similar range. Differences in peak positions may be accounted for by generic differences in the overall polarization of the cell. Interestingly, in the present study, the anode consists of ~10 μm Fe_2O_3 nanowires without any additional conductive agents but display relatively low polarization. Fig. 2c shows the galvanostatic charge and discharge of the electrode at 0.1 C. The single sloping plateau exists in the first lithiation cycle, but appears as two distinct plateaus in subsequent cycles. The difference may result from a source of polarization in the first cycle that is not present in the second cycle.

Fig. 3a–l shows the TEM micrographs and SAED patterns from Fe_2O_3 nanowires at various stages of lithiation. Beginning at 0.9 V, a thin surficial layer forms that relates to solid electrolyte interphase (SEI) formation. The SAED pattern still exhibits prominent single crystal diffraction spots with very weak diffraction rings, indicating limited conversion reaction has occurred at this point. At 0.8 V, bright-field TEM imaging reveals a moderate density of dark spots distributed about the nanowires, which were confirmed by the dark field TEM to be ~4.3 ± 0.3 nm nanocrystals. Corresponding
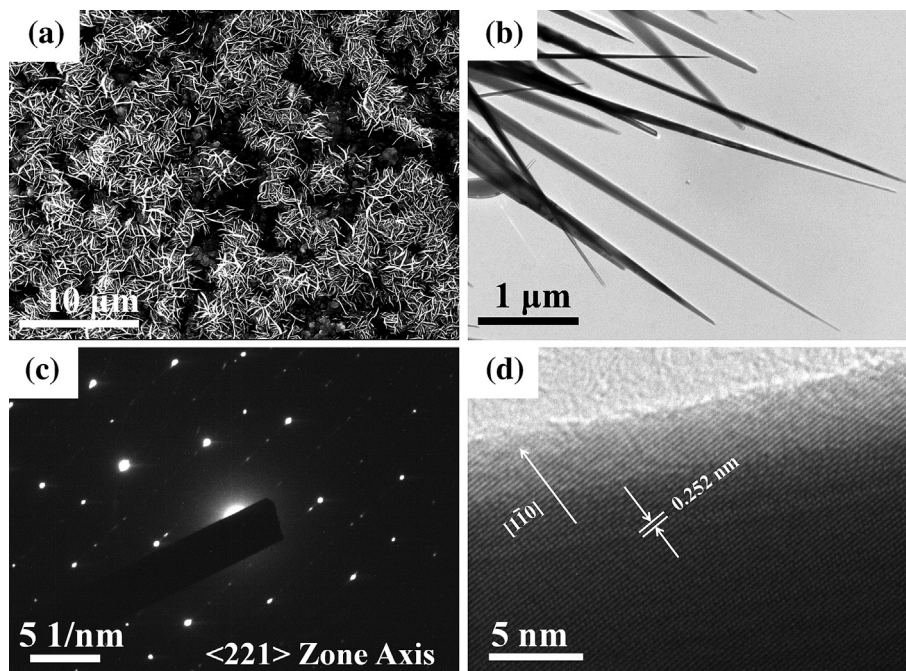
Fig. 1. As grown α-Fe$_2$O$_3$ nanowires image by SEM (a) TEM (b), selected area electron diffraction (c), and high-resolution imaging (d).

SAED rings can be indexed to Fe$_3$O$_4$. After further cycling to 0.7 V, an increased density of nanocrystals emerges throughout the nanowire, with little change in their average size of 4.1 ± 0.4 nm. These spots are still indexed as Fe$_3$O$_4$, as shown in Fig. 3i. After lithiation to 0.6 V, the average size of the nanocrystals decreases to 2.9 ± 0.2 nm. At this stage, BCC Fe exists as the only phase in the diffraction pattern. After lithiation to 0.5 V, a thick SEI layer forms and the average diameter of the nanowires increases encase the nanowires. The dark field imaging reveals a uniform dispersion of nanocrystals throughout the nanowire and their size sharply increases to 21 ± 1.7 nm. The samples are subsequently delithiated by cycling to 2 V and holding for 3 h. As shown in Fig. 4, the nanocrystalline Fe is reoxidized, producing nanocrystalline Fe$_2$O$_3$ with an average size of 7.7 ± 0.8 nm. The nanowire morphology continues after delithiation and was found to persist to 30 cycles (Fig. 5). The stability of the nanostructures likely results from the small volume change and the localization of mass transport associated with the conversion reaction. Fig. 6 shows the capacity retention over several cycles. Some capacity fade is observed. Portions of the oxide nanowire layer were observed to debond from the underlying Fe wire, which may account for much of the capacity

fade. Significant SEI growth may account for differences in capacity between the first and subsequent cycles.

A sample held at constant potential of 0.1 V for 3 h was subsequently characterized by STEM. The element distribution across the lithiated nanowire was analyzed by EELS as shown in Fig. 7. Carbon detected across the entire nanowire relates to the organic components of the SEI. The signal from lithium is relatively uniform across the nanowire. Although signals from iron and oxygen cannot be collected in the core area due to the increasing thickness, which affects the signal to noise ratio, the tendency can be seen that the Fe/O intensities are gradually enriched from the edge to the core of the nanowire. Similarly, the Z-contrast STEM image suggests that the nanowire, after complete lithiation, has a core/shell structure. The shell part primarily consists of light elements, which include Li/O/C from the SEI. The core contains O, Li, Fe, and C, but some of the light element contribution may result from the projection of the shell region. These results indicate that lithium ions diffuse into the Fe$_2$O$_3$ nanowire, while Fe and O, which have much lower diffusivities, remain within the initial nanowire boundaries. This could also explain the persistence of the nanowire geometry over multiple cycles without geometric changes.
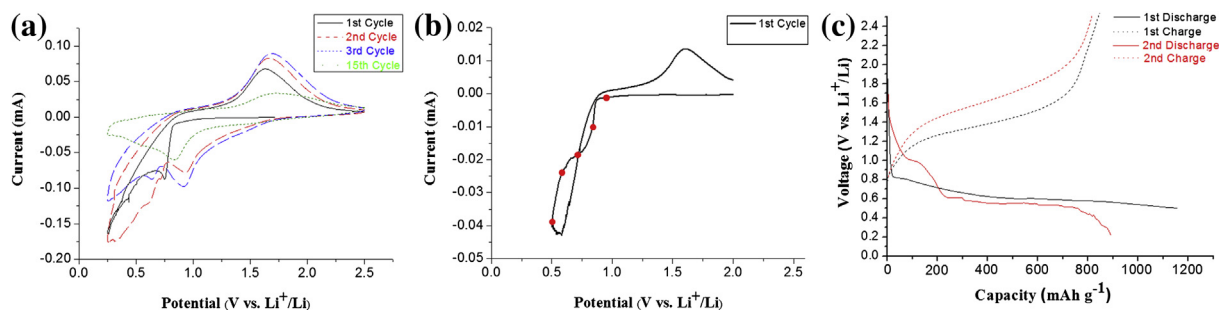

Fig. 2. Cyclic voltammagrams for the lithiation and delithiation of α-Fe$_2$O$_3$ nanowires cycled against Li metal at scan rates of 500 μV s^{-1} (a), and 50 μV s^{-1} (b). (c) The first and second charge and discharge profiles for an electrode cycled at 0.1 C.
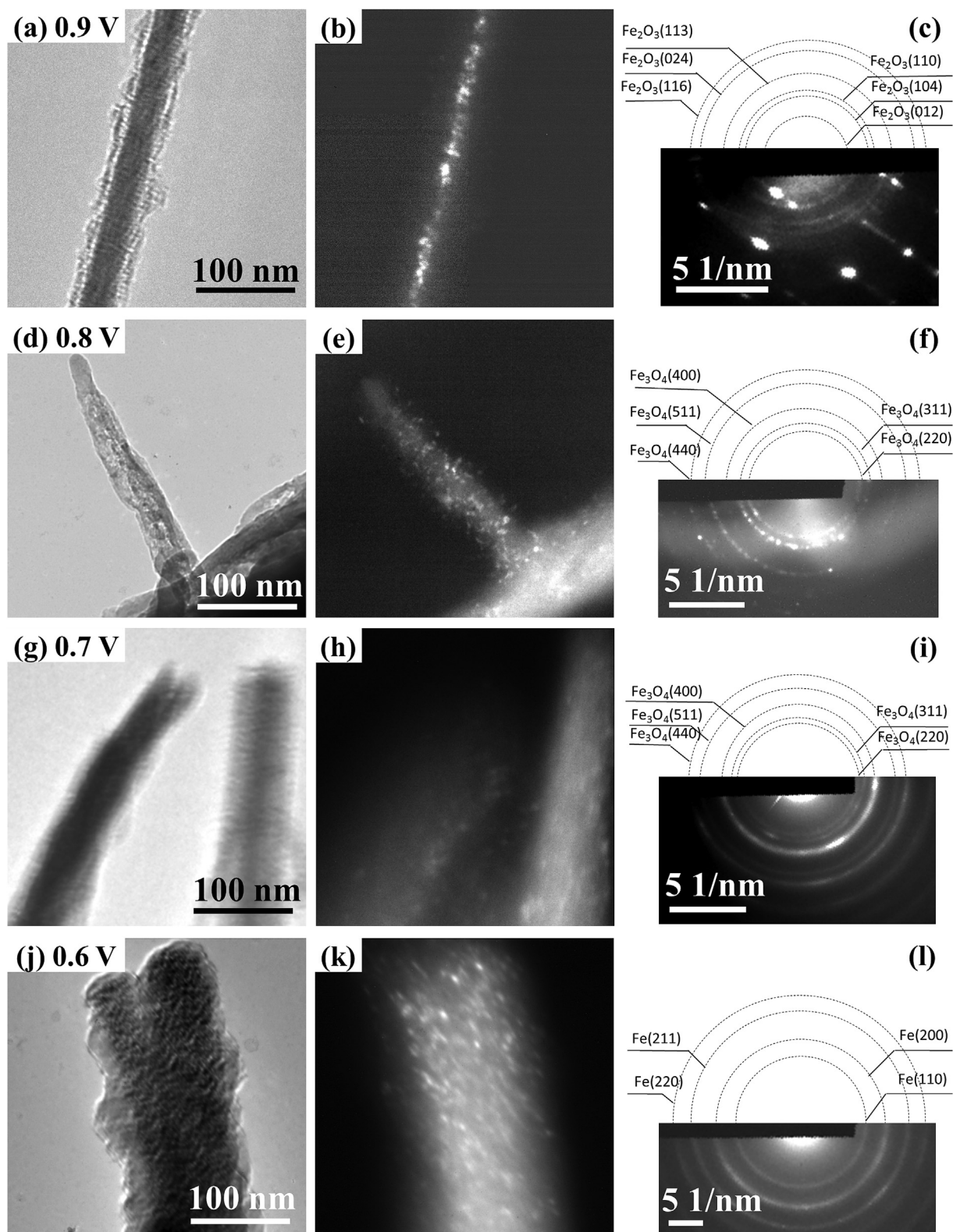
Fig. 3. (left) Bright field TEM images, (middle) dark field TEM images, and (right) SAED patterns of α-Fe₂O₃ nanowire discharged to 0.9, 0.8, 0.7 and 0.6 V.

The Fe₃O₄ nanocrystals precipitate with average size of 4.3 nm. Their size does not increase with further reaction, but instead their number density increases. The phenomenon likely results from limits on continued reaction due to solid-state diffusivity and a lack of coarsening that is also limited by diffusion. The appearance of Fe nanocrystals at 0.6 V accompanies a ∼30% reduction in nano-particle size to 2.9 nm. The loss of oxygen from individual Fe₃O₄ particles can account for this size reduction. Our measurement of nanocrystal size is reasonably consistent with the simulation of the FeF₃ system (2–3 nm) [23]. After cycling to 0.5 V, a pronounced
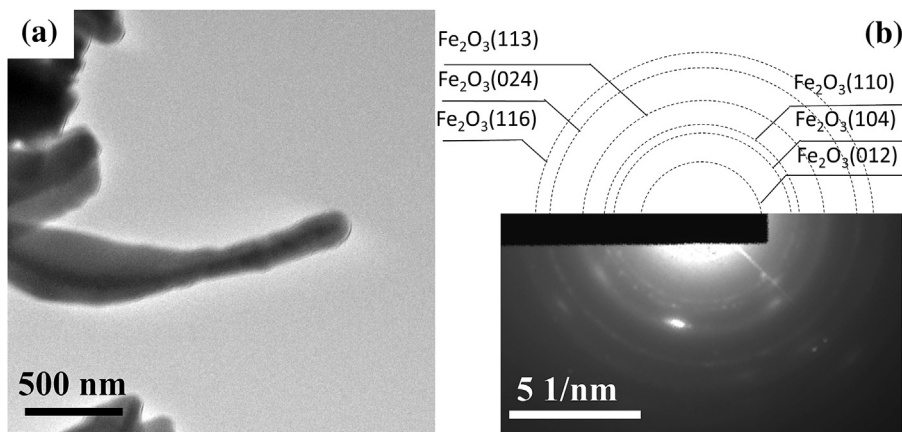
Fig. 4. Bright field TEM image and SAED pattern of α-Fe₂O₃ nanowire after complete lithiation and subsequent delithiation at 2 V (a), and the corresponding SAED (b).
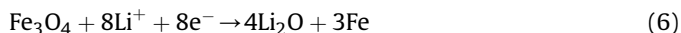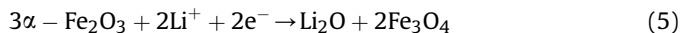
increase in grain size to 21 nm occurs. The two-phase microstructure likely limits coarsening and grain growth. The Fe particle size should increase due to propagation of the reaction fronts. After charging to 2.0 V, the particle size decreases again to 7.7 nm. During lithiation and conversion of Fe_xO to Feo, diffusion of $Fe^{2+/3+}$ out of Fe_xO likely limits the reaction, while $Fe^{2+/3+}$ diffusion into Li_2O likely limits the delithiation process. The difference in characteristic particle sizes results from the difference in the Fe cation diffusivities in these two oxides.

XRD performed on nanoparticle-based composite electrodes support the general phase evolution observed in the nanowire samples (Fig. 8). When 1 lithium per Fe_2O_3 formula unit is inserted, Fe_3O_4 appears as the primary phase in the XRD pattern. Insertion of additional Li reduces the fraction of Fe_3O_4, while the fraction of BCC iron increases. $Li_2Fe_2O_3$ has been suggested as an intermediate in the reaction sequence [18]. $Li_2Fe_2O_3$ shares several similar diffraction peaks with Fe_3O_4 but may be distinguished by Fe_3O_4 peaks that occur at 29.8°, 53.1°, and 56.2°.

α-Fe₂O₃ electrically insulates well at room temperature (electron conductivity $\sigma \sim 10^{-8}$ S m^{-1}) [24]. Charge transport across ∼10 μm of this material is significant. However, the polarization in CV is smaller than that reported for nanoparticles in conventional coin cells with conductive agents present [16,21]. Surface transport may facilitate the initial reaction, which results in the formation of the Fe_3O_4, which displays significantly higher electron conductivity ($\sigma \sim 10^{-2}$ S m^{-1}) [25]. An increase in the amount of charged defects and interfaces during the first cycle could account for the reduction in polarization observed in the first few cycles (Fig. 2a).

The overall results for the phase evolution during lithiation and delithiation of α-Fe₂O₃ nanowires characterized by TEM differ from those obtained for nanoparticles characterized by XRD. The reaction sequence determined here follows;

$$3\alpha - Fe_2O_3 + 2Li^+ + 2e^- \rightarrow Li_2O + 2Fe_3O_4 \qquad (5)$$

$$Fe_3O_4 + 8Li^+ + 8e^- \rightarrow 4Li_2O + 3Fe \qquad (6)$$

The two plateaus observed in the galvanostatic discharge profile support a two-step lithiation process. The source of the difference between this mechanism and previous reports is unclear, but it may relate to the difference in sample geometry or testing conditions. The larger nanowires may not be able to accommodate a strained lattice necessary to support α-LiFe₂O₃. This may alter the subsequent phase evolution as the nanowires initially form Fe_3O_4 nanoparticles as a result of the conversion reaction. The system investigated by Larcher et al. initially refined its crystallite size through the formation of $Li_2Fe_2O_3$ [18]. $Li_2Fe_2O_3$ and Fe_3O_4 are
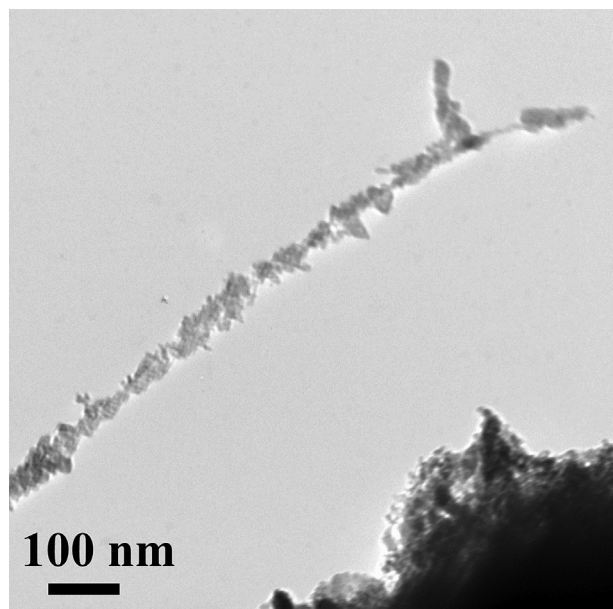

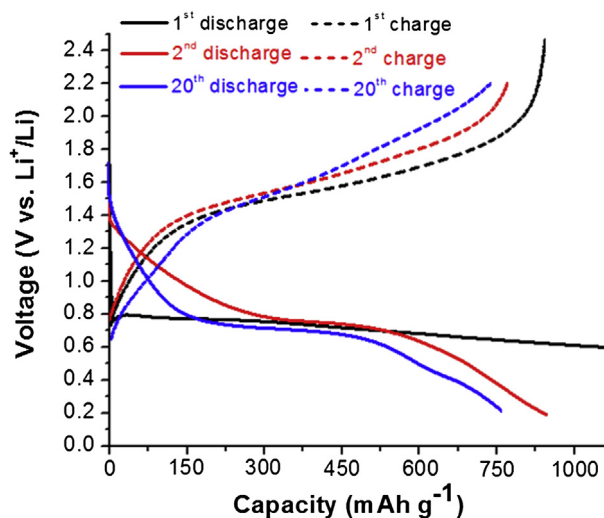**Fig. 5.** Bright field TEM image of a Fe₂O₃ nanowire after 30 cycles.

Fig. 6. Voltage vs. capacity profiles of α-Fe₂O₃ nanowires cycled at 0.2 C.
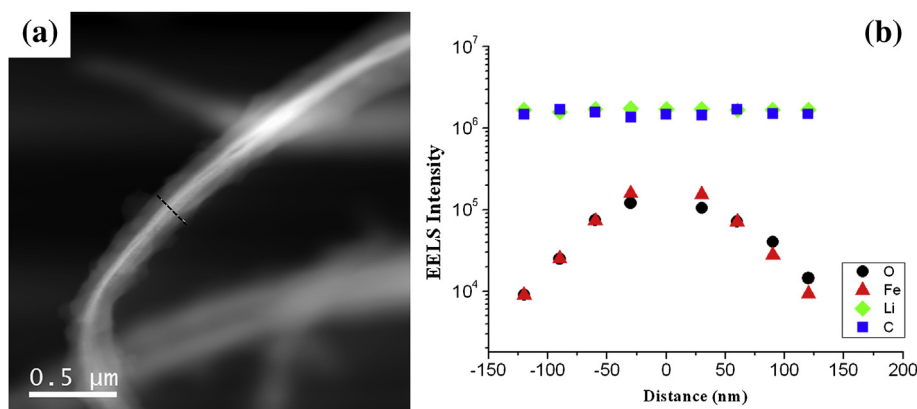
Fig. 7. Integrated peak counts from EELS as a function of distance across a lithiated nanowire. Data taken from region indicated in image.
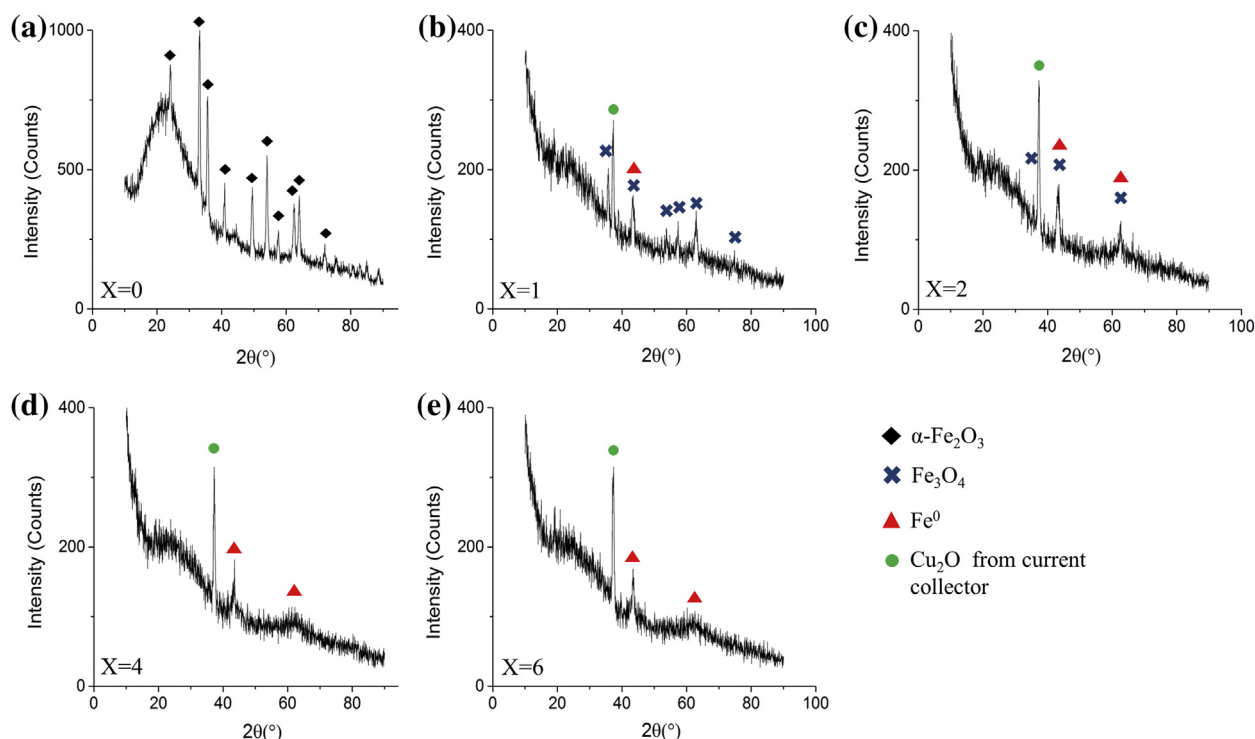

Fig. 8. XRD patterns collected intermittently during the discharge of a Li/α-Fe$_2$O$_3$ cell. The values of X indicate the number of lithium ions per formula unit.

clearly differentiated by diffraction, thus the evolution of these two systems is believed to be distinct. In the final stage, both systems result in Fe nanocrystals and Li$_2$O.

4. Conclusions

Lithiation of single crystal Fe$_2$O$_3$ nanowires proceeds by the initial reduction to Fe$_3$O$_4$ nanoparticles, and subsequent reduction to BCC Fe^0. Both processes produce Fe-based reaction products in the form of nanocrystals and Li$_2$O. During delithiation the Fe^0 reverts to Fe$_2$O$_3$. The delithiated electrode maintains the nanowire geometry over many cycles due to the nature of the short-range cation diffusion that facilitates the process.

References

[1] J.B. Goodenough, Y. Kim, Chem. Mater. 22 (2010) 587.
[2] M. Ogasa, IEEJ Trans. Electr. Electron. Eng. 3 (2008) 15.
[3] Z. Yang, J. Zhang, M.C. Meyer, X. Lu, D.W. Choi, J.P. Lemmon, J. Liu, Chem. Rev. 111 (2011) 3577.
[4] D. Linden, Handbook of Batteries, second ed., McGraw-Hill, New York, 1985.
[5] J.R. Owen, Chem. Soc. Rev. 26 (1997) 259.
[6] C. Daniel, JOM 60 (2008) 43.
[7] A.K. Shukla, T.P. Kumar, Curr. Sci. 94 (2008) 314.
[8] P. Arora, R.E. White, M. Doyle, J. Electrochem. Soc. 145 (1998) 3647.
[9] J. Christensen, J. Newman, J. Solid State Electrochem 10 (2006) 293.
[10] Y. Shao-Horn, S.A. Hackney, A.J. Kahaian, K.D. Kepler, E. Skinner, J.T. Vaughey, et al., J. Power Sources 81 (1999) 496.
[11] P. Poizot, S. Laruelle, S. Grugeon, L. Dupont, J.M. Tarascon, Nature 407 (2000) 496.
[12] H. Wu, J. Chen, H. Hng, X.W. Lou, Nanoscale 4 (2012) 2526.
[13] L. Lu, H.-Z. Kou, W. Mo, H. Liu, Y. Wang, J. Phys. Chem. B 110 (2006) 15.

[14] S.U.M. Khan, J. Akikusa, J. Phys. Chem. B 103 (1999) 7184.
[15] T. Yu, Y. Zhu, X. Xu, K.S. Yeong, Z. Shen, P. Chen, C.T. Lim, J.T.L. Thong, C.H. Sow, Small 2 (2006) 80.
[16] J. Chen, L. Xu, W. Li, X. Gou, Adv. Mater. 17 (2005) 582.
[17] J. Sarradin, A. Guessous, M. Ribes, J. Power Sources 62 (1996) 149.
[18] D. Larcher, C. Masquelier, D. Bonnin, Y. Chabre, V. Masson, J.-B. Leriche, J.-M. Tarascon, J. Electrochem. Soc. 150 (2003) A133.
[19] J. Morales, L. Sánchez, F. Martín, F. Berry, X. Ren, J. Electrochem. Soc. 152 (2005) A1748.
[20] D. Larcher, D. Bonnin, I. Rivals, L. Personnaz, J.-M. Tarascon, J. Electrochem. Soc. 150 (2003) A1643.
[21] M.V. Reddy, T. Yu, C.-H. Sow, Z. Shen, C.T. Lim, G.V. Subba Rao, B.V.R. Chowdari, Adv. Funct. Mater. 17 (2007) 2792.
[22] A.G. Nasibulin, S. Rackauskas, H. Jiang, Y. Tian, P.R. Mudimela, S.D. Shandakov, L. Nasibulina, J. SainioM, E.I. Kauppinen, Nano Res. 2 (2009) 373.
[23] Y. Ma, S.H. Garofalini, J. Am. Chem. Soc. 134 (2012) 8205.
[24] S. Ito, Y. Yui, J. Mizuguchi, Mater. Trans. 51 (2010) 1163.
[25] E.J.W. Verwey, P.W. Haayman, Physica 8 (1941) 979.